Journal of
Applied and Computational Mechanics

Shahid Chamran University of Ahvaz

Research Paper

Thermal–Aerodynamic Performance Measurement of Air Heat Transfer Fluid Mechanics over S-shaped Fins in Shell-and-tube Heat Exchangers

Ali J. Chamkha[1], Younes Menni[2], Houari Ameur[3]

[1] Faculty of Engineering, Kuwait College of Science and Technology, Doha, Kuwait, Email: a.chamkha@kcst.edu.kw

[2] Unit of Research on Materials and Renewable Energies, Department of Physics, Faculty of Sciences, Abou Bekr Belkaid University BP 119-13000-Tlemcen, Algeria, Email: menniyounes.cfd@gmail.com

[3] Department of Technology, University Center of Naama, Po. Box 66, Naama 45000, Algeria, Email: Houari_ameur@yahoo.fr

Abstract. Forced-convection heat transfer of pure air-fluid inside an open channel as a section of a shell-and-tube heat exchanger is evaluated numerically. S-shaped obstacles are used in the mentioned channel. Airflow inside the channel is considered as a turbulence flow. Governing equations are solved throughout the computational Finite Volume Method (FVM). These equations are analyzed using the standard k-ε model. The results are designed based on the geometry of S-shaped obstacles. Mentioned results are shown in the form of turbulent kinetic energy (k), turbulent intensity (TI), turbulent viscosity (μ_t), temperature (T), Nusselt numbers (Nu_x local, and Nu average), friction coefficients (Cf local, and f average), and the thermal aerodynamic performance factor (TEF), for a Reynolds number (Re) of 12,000 to 32,000. This type of analysis is very useful in many industries and engineering-related problems for getting a good idea about the physical model whenever the analytic solution is out of reach.

Keywords: Shell-and-tube heat exchanger, Thermal performance, Fluid mechanics, Turbulent flow, Numerical simulation.

1. Introduction

A disadvantage of smooth ducts, such as those found in solar collectors or shell-and-tube heat exchangers, is that they have poor thermal performance. One of the old effective ways to improve the thermal enhancement factor of such channels is to insert the fins into the heat transfer fluid stream. This technique has been prevalent today because of its importance by improving the structure of the channel internally. Through this technique, fins can be added inside the channel in staggered [1], transverse [2], continuous [3], discrete [4], solid [5], perforated [6], porous [7], vertical [8], inclined [9], with simple or complex geometric shapes, defined as square [10], rectangle [11], triangle [12], drop [13], diamond [14], arc [15], segmental [16], helical [17], Delta [18], ladder-type fold [19], trisection helical [20], oblique horseshoe [21], twisted [22], Z [23], and V [24]. Some other studies have investigated the effect of fin size on thermal performance by changing their height [25] and thickness, and have also identified the best possible location [23] of the fin inside the channel. Studies have shown that the presence of fins within the channel shows an improvement in the thermal and dynamic behavior within the channel, by creating very large cells for recycling, especially on the backs of these fins, resulting in good mixing of the fluid and greater contact with the hot surfaces and thus a successful thermal transfer [26-30]. Interesting research works on the heat and mass transport in channels, ducts and tubes can be found in the referenced manuscripts (Zhao et al. [31], Zhai et al. [32], Guervilly et al. [33], Yu et al. [34], Dutta and Kundu [35], Korichi and Oufer [36], Herman and Kang [37], Read [38], Manca et al. [39], Ndlovu [40], Ooi et al. [41], Ortiz et al. [42], Singh and Dhiman [43], Singh [44], and Saleh et al. [45]).

In order to improve the thermal performance of heat exchanger channels or those in the solar receptors, a new design should be sought, that aims to give a new flow structure, by eliminating dead areas, and creating cells for recycling, in order to increase the heat transfer with the hot surfaces. In the majority of previous studies, the authors used only channels with simple flat obstacles. For this raison, this paper proposes a new design for the baffled channels, by inserting fins of a very complex geometrical shape, such as the form 'S', and studying their effect on turbulence phenomena using a CFD technique (computational fluid dynamics). Different fields of turbulent kinetic energy (k), turbulent intensity (TI), turbulent viscosity (μ_t), and temperature (T), as well as various normalized heat transfer rate curves and friction and performance profiles have been identified with the suggestion of new ideas to be embodied in the future.
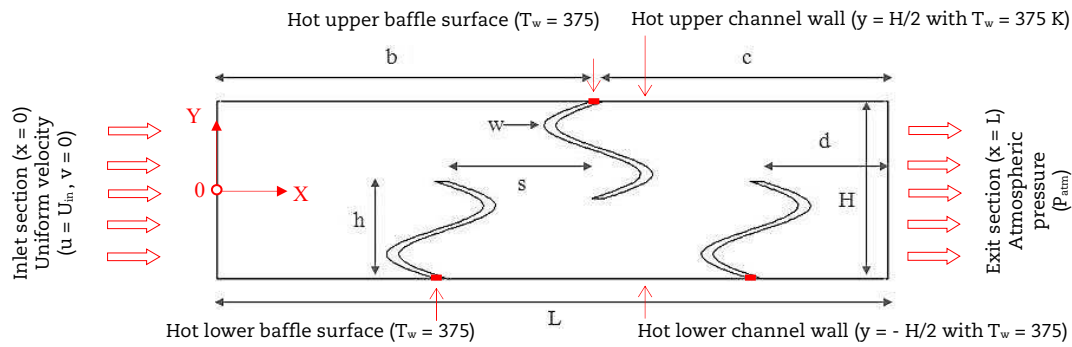
Fig. 1. Geometrical model with: H = 0.146m, L = 0.554m, w = 0.01m, h = 0.08m, s = 0.12m, b = 0.31m, c = 0.234m, d = 0.104m and Dh = 0.167m.

2. Computational Domain

The problem under study contains a numerical analysis of a specific shell-and-tube exchanger channel, with complex geometry fins. The problem solved is potentially interesting for researchers and engineers working on solar collectors and aerospace industry. It is known that thermal aerodynamic performance enhancement can be achieved by creating longitudinal vortices in the field of the flow. These vortex cells can be generated by 'S'-shaped fins, and a numerical study of such heat exchanger channels is not a simple task. Therefore, we used a present-day Commercial CFD technique to solve the problem.

Forced convection of a pure fluid (air) in a heat exchanger under turbulent flow condition is evaluated. For this purpose, a channel (or duct) from the heat exchanger is considered. Three modern and intricately shaped baffles (of S-form), intertwined within the channel are present to create turbulence and generate recycling cells for better heat exchange, see Fig. 1. The mathematical equations governing the flow and energy can be written in the common form as

$$\frac{\partial}{\partial \mathbf{x}}(\rho u \varphi) + \frac{\partial}{\partial \mathbf{y}}(\rho v \varphi) = \frac{\partial}{\partial \mathbf{x}}\left[\Gamma_{\varphi} \frac{\partial \varphi}{\partial \mathbf{x}}\right] + \frac{\partial}{\partial \mathbf{y}}\left[\Gamma_{\varphi} \frac{\partial \varphi}{\partial \mathbf{y}}\right] + S_{\varphi} \tag{1}$$

where
$\phi \equiv$ (u, v, k, ε and T),
u: x-velocity,
v: y-velocity,
k: turbulent kinetic energy,
ε: turbulent dissipation rate,
Γ_{ϕ}: turbulent diffusion coefficient, and
S_{ϕ}: source term.

Equations for ϕ, Γ_{ϕ} and S_{ϕ}:

Fluid mass conservation:

$$\varphi = 1 \tag{2}$$

$$\Gamma_{\varphi} = 0 \tag{3}$$

$$S_{\varphi} = 0 \tag{4}$$

X-direction fluid momentum conservation:

$$\varphi = v \tag{5}$$

$$\Gamma_{\varphi} = \mu_e \tag{6}$$

$$S_{\varphi} = \frac{\partial P}{\partial y} + \frac{\partial}{\partial x}\left[\mu_e\left(\frac{\partial u}{\partial y}\right)\right] + \frac{\partial}{\partial y}\left[\mu_e\left(\frac{\partial v}{\partial y}\right)\right] \tag{7}$$

Y-direction fluid momentum conservation:

$$\varphi = v \tag{8}$$

$$\Gamma_{\varphi} = \mu_e \tag{9}$$

$$S_{\varphi} = \frac{\partial P}{\partial y} + \frac{\partial}{\partial x}\left[\mu_e\left(\frac{\partial u}{\partial y}\right)\right] + \frac{\partial}{\partial y}\left[\mu_e\left(\frac{\partial v}{\partial y}\right)\right] \tag{10}$$

Fluid energy conservation:

$$\varphi = T \tag{11}$$

$$\Gamma_\varphi = \frac{\mu_e}{\sigma_T} \tag{12}$$

$$S_\varphi = 0 \tag{13}$$

Kinetic energy of turbulence:

$$\varphi = k \tag{14}$$

$$\Gamma_\varphi = \mu_l + \frac{\mu_t}{\sigma_k} \tag{15}$$

$$S_\varphi = -\rho\varepsilon + G_k \tag{16}$$

Rate of dissipation of turbulence:

$$\varphi = \varepsilon \tag{17}$$

$$\Gamma_\varphi = \mu_l + \frac{\mu_t}{\sigma_\varepsilon} \tag{18}$$

$$S_\varphi = \frac{\varepsilon}{k}\left(C_{1\varepsilon}G_k - C_{2\varepsilon}\rho\varepsilon\right) \tag{19}$$

where

$$\mu_{eff} = \mu_l + \mu_t \tag{20}$$

$$\mu_t = f_\mu \rho C_\mu \frac{k^2}{\varepsilon} \tag{21}$$

$$G_k = \mu_t \left\{ 2\left[\left(\frac{\partial u}{\partial x}\right)^2 + \left(\frac{\partial v}{\partial y}\right)^2\right] + \left(\frac{\partial u}{\partial y} + \frac{\partial v}{\partial x}\right)^2 \right\} \tag{22}$$

and

$$C_{1\varepsilon} = C_{3\varepsilon} = 1.44,\ C_{2\varepsilon} = 1.92,\ C_\mu = 0.09,\ \sigma_k = 1.0,\ \sigma_\varepsilon = 1.3,\ \text{and}\ \sigma_T = 0.85 \tag{23}$$

representing the constant values of the standard *k-ε* model, reported by Launder and Spalding [46]. The current boundary conditions are presented as:

For the channel inlet section, at x = 0:

$$u = U_{in} \tag{24}$$

$$v = 0 \tag{25}$$

$$T = T_{in} = 300K \tag{26}$$

$$k_{in} = 0.005U_{in}^2 \tag{27}$$

$$\varepsilon_{in} = 0.1k_{in}^2 \tag{28}$$

For the entire channel walls, upper wall at y = H/2 and lower wall at y = -H/2:

$$u = v = 0 \tag{29}$$

$$k = \varepsilon = 0 \tag{30}$$

$$T = T_w = 375K \tag{31}$$

For the fluid/solid interface:

$$T_f = T_s \tag{32}$$

$$\lambda_f \frac{\partial T_f}{\partial n} = \lambda_s \frac{\partial T_s}{\partial n} \tag{33}$$

For the channel exit section, at x = L:

$$P = P_{atm} \tag{34}$$

$$\frac{\partial \varphi}{\partial x} = 0 \tag{35}$$

Dimensionless parameters:

Reynolds number (Re):

$$\mathrm{Re} = \rho \bar{U} D_h / \mu \tag{36}$$

Hydraulic diameter (D_h):

$$D_h = 2HW/(H + W) \tag{37}$$

Skin friction coefficient (Cf):

$$C_f = \frac{2\tau_w}{\rho \bar{U}^2} \tag{38}$$

Friction factor (f):

$$f = \frac{2(\Delta P/L)D_h}{\rho \bar{U}^2} \tag{39}$$

Local Nusselt number (Nu_x):

$$Nu_x = \frac{h(x).D_h}{\lambda_f} \tag{40}$$

The average Nusselt number (Nu):

$$Nu = \frac{1}{L} \int Nu_x \partial x \tag{41}$$

The thermal enhancement factor (TEF):

$$TEF = (Nu/Nu_0)/(f/f_0)^{1/3} \tag{42}$$

Dittus and Boelter correlation [47]:

$$Nu_0 = 0.023 \, \mathrm{Re}^{0.8} \, \mathrm{Pr}^{0.4} \tag{43}$$

Petukhov correlation [48]:

$$f_0 = (0.79 \ln \mathrm{Re} - 1.64)^{-2} \tag{44}$$

where
τ_w: wall shear stress,
U: average axial velocity,
ΔP: pressure drop,
Nu_0: average Nusselt number for smooth channel,
f_0: friction factor for smooth channel, and
h_x: local convective heat transfer coefficient.

3. Numerical Resolution

The mathematical equations, governing the flow and energy, are solved numerically by using:

- Finite Volume Method (FVM) of Patankar [49],
- SIMPLE discretization algorithm of Patankar [49],
- QUICK numerical scheme of Leonard and Mokhtari [50], and
- ANSYS FLUENT software [51].

In addition, a tetrahedral type mesh was used along the studied channel, as shown in Fig. 2. The curves in Fig. 3 are a comparison of pressure coefficient (P) and axial velocity (u) values obtained in the present simulation with that of the numerical and experimental values provided by Demartini et al. [11]. This comparison was made by relying on the same flow and geometry conditions reported by the referenced paper [11], which gave the same behavior both quantitatively and qualitatively, and this indicates the validity of the simulation used in this research work. Also, there is a preview of the heat exchange values in terms of average Nusselt number (Nu_0) as well as the pressure drop in terms of friction faction (f_0) in the case of the smooth channel by relying on some experimental correlations [47,48] as shown in Fig. 4. The effect of changing the turbulence model is also shown in the following figure by comparing four known models, which are as follows: standard *k-ε*, RNG *k-ε*, standard *k-ω*, and SST *k-ω* turbulence models. This comparison demonstrated the importance of the standard *k-ε* first turbulence model, which gives good values, in comparison with the other models, basing on the experimental data presented by Demartini et al. [11], see Fig. 5. Finally,

the density of the mesh nodes has been validated, by proposing a group of ($N_x \times N_y$) pairs, i.e., (95 × 35), (120 × 45), (145 × 55), (170 × 65), (195 × 75), (220 × 85), (245 × 95), and (370 × 145), and comparing their effects on the numerical solution to the u/U_{in} value, highlighting the (245 × 95) pair as a better density for an optimal solution, see Fig. 6.
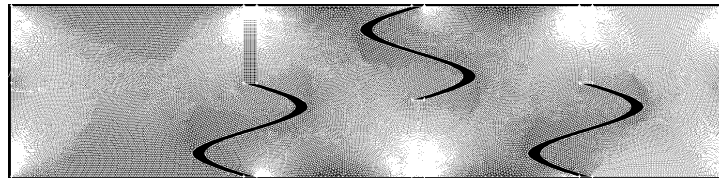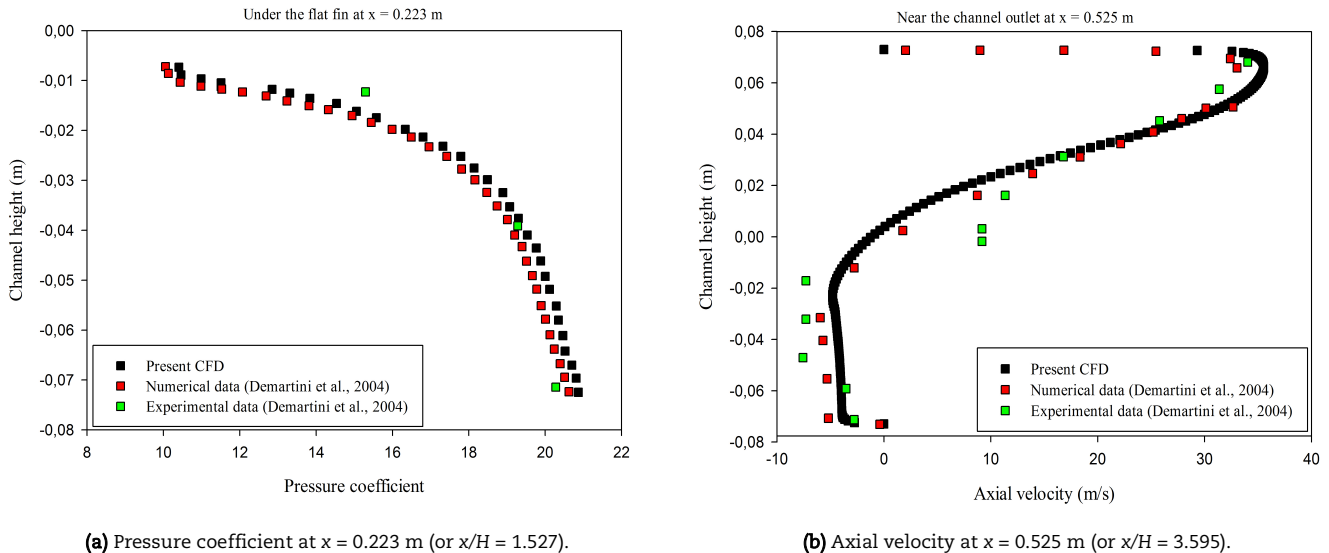

Fig. 2. Used mesh.

(a) Pressure coefficient at $x = 0.223$ m (or $x/H = 1.527$).

(b) Axial velocity at $x = 0.525$ m (or $x/H = 3.595$).

Fig. 3. Validation of the present profiles of pressure coefficient and axial velocity with the referenced data [11], under the following condition: channel with staggered two baffle plates [11], air fluid, and $U_{in} = 7.8$ m/s
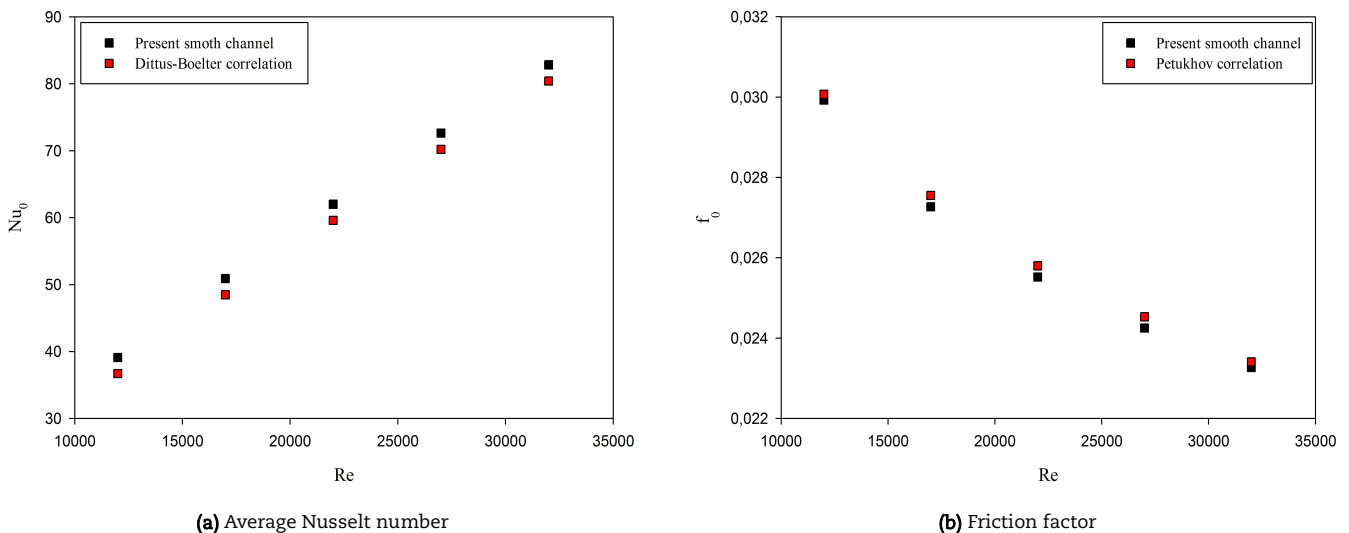

(a) Average Nusselt number

(b) Friction factor

Fig. 4. Verification of the average values of Nusselt number and friction factor for the present smooth channel with the referenced correlations [89,90], $Re = 12{,}000 - 32{,}000$.

4. Results and Discussion

In this simulation, the thermal optimization of thermal exchange channels is the object of the study, through a thermal analysis, of turbulent air inside a rectangular channel with modern and complex geometry baffles of S-type. Different flow fields and T profiles, as well as various normalized heat transfer and friction coefficient profiles, and performance curves have been identified with the suggestion of new ideas to be embodied in the future. Fig. 7 shows the k fields for different Re values, varying from 12,000 to 32,000. The k values are very high for large values of Re. This increase appears in the case of $Re = 32{,}000$, above the last S-fin, near the top surface of the channel. The TI fields are also shown in the same Figure. The values of TI are located on a wide area from the channel, compared to k fields, and for large values of Re. These large values are located at the top region of the channel, near its exit. Moreover, there is a correlation between the values of TI and Re.
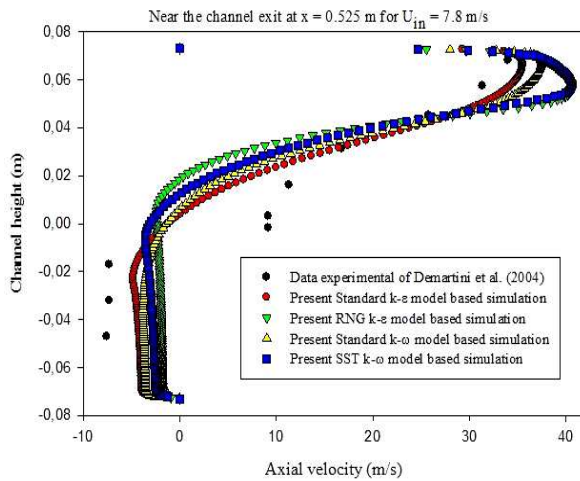
Fig. 5. Effects of turbulence models on the axial velocity at $x = 0.525$ m (or $x/H = 3.595$) for $U_{ni} = 7.8$ m/s.
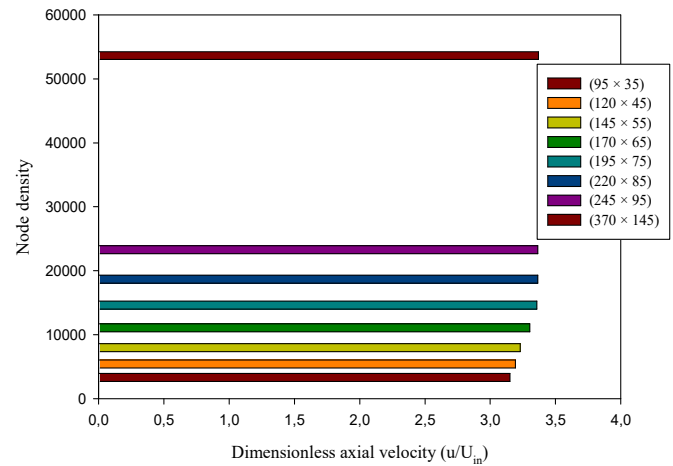

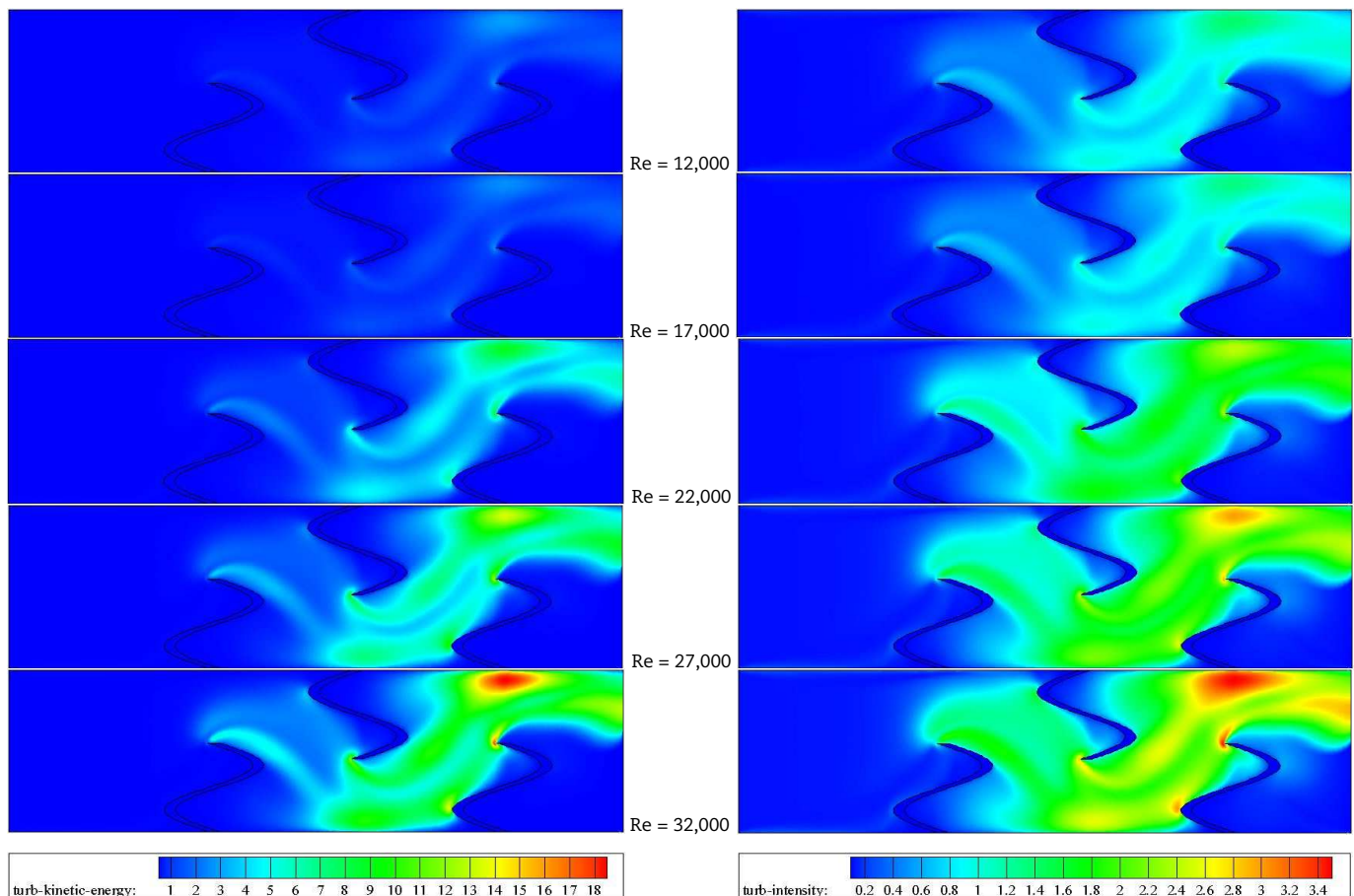**Fig. 6.** Effects of mesh node densities on the maximum u/U_{in} values for $Re = 12,000$.

Fig. 7. Fields of k and TI for various Re values. Note: TI values × 100.

The effect of Re values on the μ_t fields is shown in Fig. 8. The μ_t values gradually improve with the improvement of Re values. As previously mentioned in Fig. 7 of the k and TI fields, the maximum μ_t values are also present in the same region, centered near the top surface of the channel, above the top edge of the third S-fin, in the last section of the channel. The thermal factor is also taken up in this figure, by representing the temperature fields, along the channel, and for the range of the Re previously adopted. The T is high in the vicinity of the S-fins, especially on their rear sides, where the recycling cells are located. The T decreases with increasing Re. Whereas, T gradients are optimized for large values of Re. The T gradients are high above the S-fins where the three gaps are located across the channel. While these gradients of T drop behind the S-fins and on their front sides.

Fig. 9 represents the fluid temperature profiles at the channel entrance in axial positions $x = 0.105$ m and $x = 0.135$ m, adjacent to the left side of the first S-baffle, mounted on the bottom wall of the channel. 0.205 m and 0.175 m from the front side of the second S-baffle, 0.335 m and 0.305 m from the front side of the third S-baffle, while 0.449 m and 0.419 m from the channel outlet, respectively. The velocity of the fluid decreases as it approaches the first S-baffle at the bottom of the channel, accompanied by a rise in temperature in each of the studied positions. While the temperature in the upper part of the channel is recorded due to the increase in velocity due to the decrease in the flow area above this same S-baffle, leading to increased pressure. The fluid temperature is increased by the fin's proximity where the recycling cells are located next to the lower front section of the mounted baffle at very low speeds and therefore a decrease in the temperature gradient.
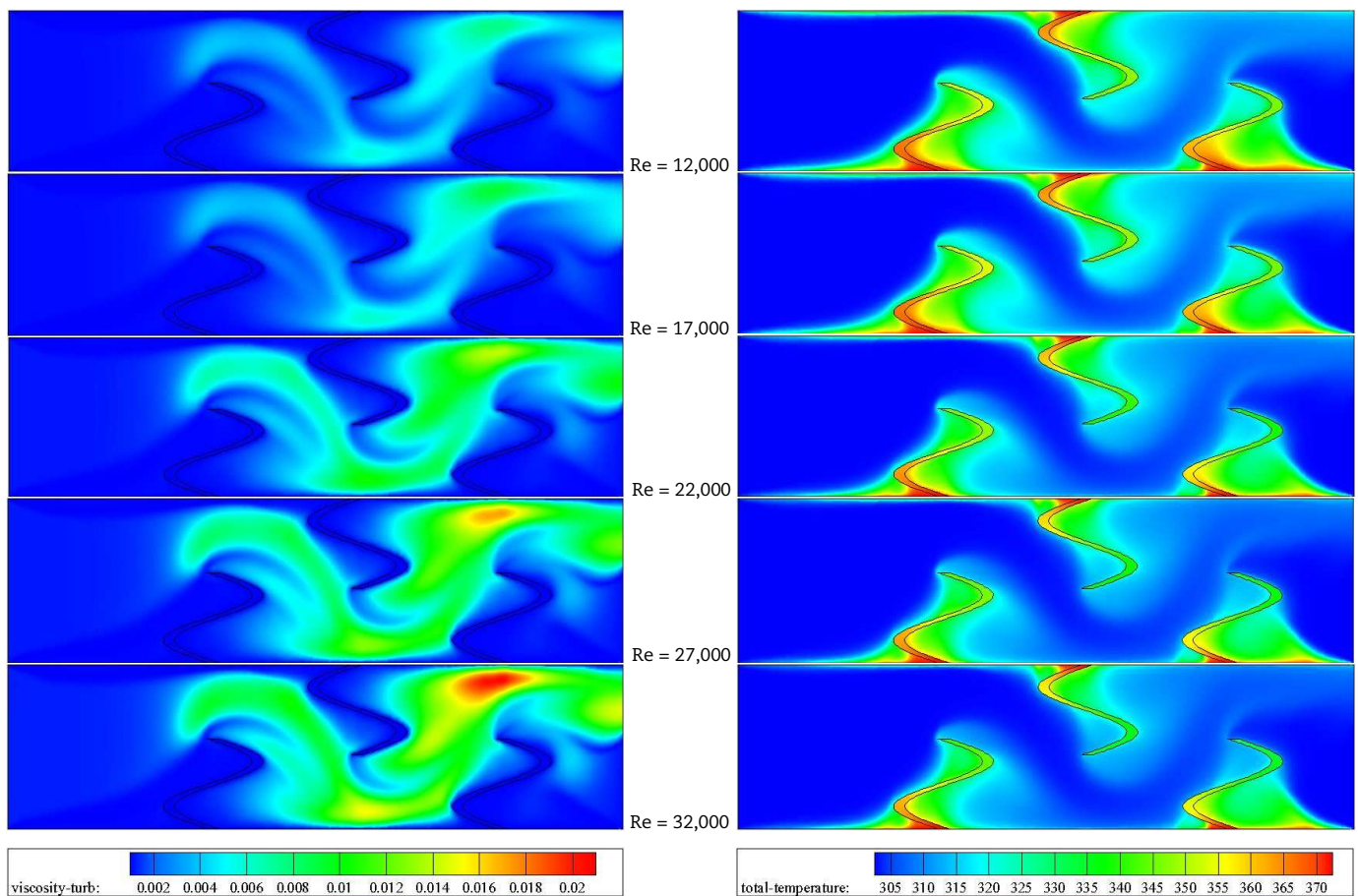
viscosity-turb: 0.002 0.004 0.006 0.008 0.01 0.012 0.014 0.016 0.018 0.02

total-temperature: 305 310 315 320 325 330 335 340 345 350 355 360 365 370

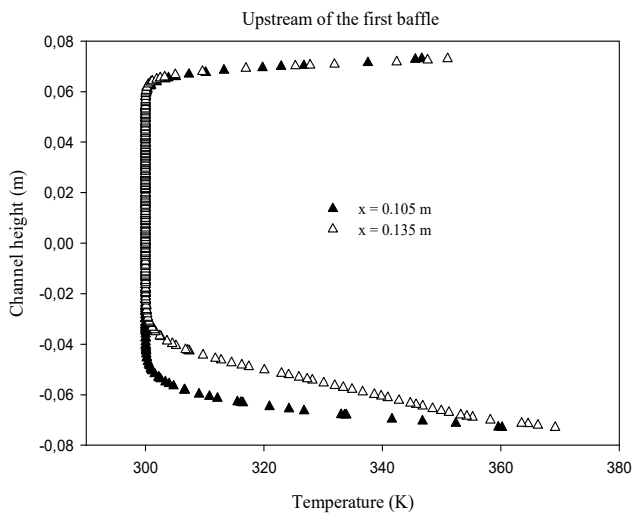**Fig. 8.** Fields of μ_t and T for various *Re* values.

Fig. 9. Profiles of *T* upstream of the first S-baffle at *x* = 0.105 m (or *x/H* = 0.719) and *x* = 0.135 m (or *x/H* = 0.924), for *Re* = 12,000.
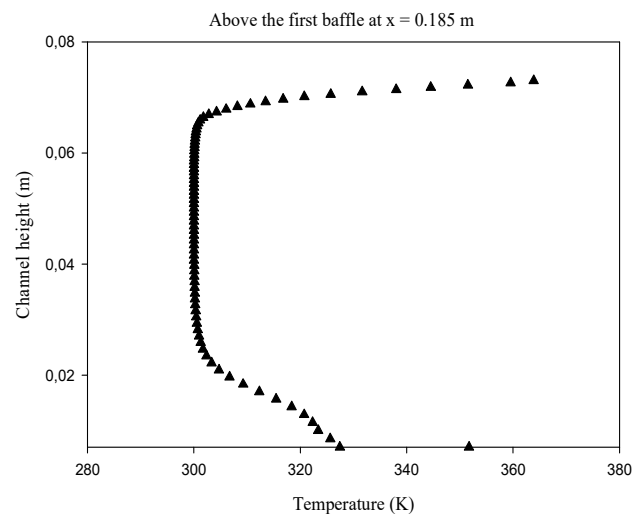
Fig. 10. Profiles of fluid temperature above the first S-baffle at *x* = 0.185 m (or *x/H* = 1.267) for Re = 12,000.

Fig. 10 represents changes in fluid temperature curves from the upper edge of the bottom first S-baffle to the bottom surface of the upper channel wall at the cross-site *x* = 0.185 m. 0.125 m and 0.255 m from the left sides of the second and third S-baffles respectively, while 0.369 m cm from the channel outlet. As shown by the figure, the temperature is very high near the top and bottom surfaces of the S-baffle and the top wall of the channel due to the low speed values in these areas due to the decrease in pressure and flow speed, while the temperature values are very low in the area confined between the two surfaces, by narrowing the flow area due to the presence of this S-fin.

The distribution of the temperature profiles of the fluid in the back of the first bottom S-baffle at the cross-section at *x* = 0.25 m is shown in Fig. 11. 0.06 m after the first S-baffle, or 0.06 m before the second S-baffle, while 0.304 m from the outlet of the channel. Temperature values are very important near the right side of the first S-baffle as a result of the decrease in flow velocity due to low pressure and form recycling cells, allowing the air current to repeat contact with hot surfaces in this area. The fluid temperature is paramount in the vicinity of the upper right half of the first S-baffle, while the temperature drops downstream over this same S-baffle. The temperature also rises near the upper surface of the S-baffle as well as in contact with the upper surface of the channel.
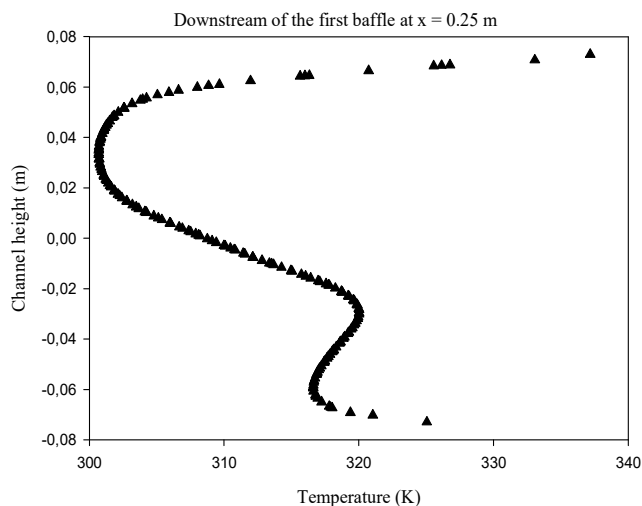
Fig. 11. Profiles of fluid temperature downstream of the first S-baffle at $x = 0.25$ m (or $x/H = 1.712$), for $Re = 12,000$.
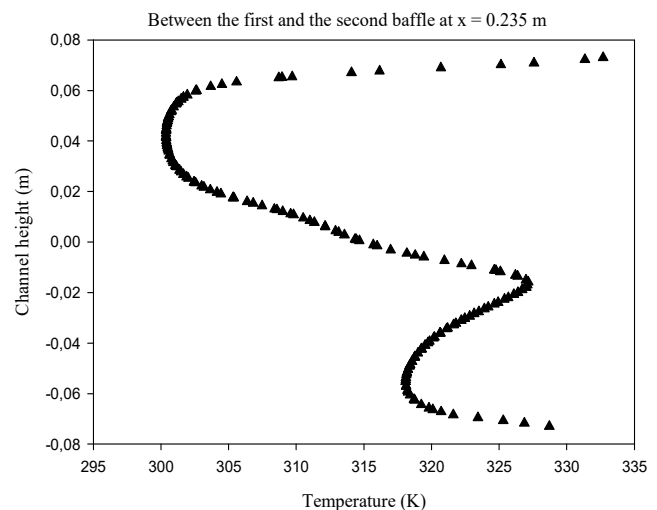

Fig. 12. Profiles of fluid temperature between the first and the second S-baffles at $x = 0.235$ m (or $x/H = 1.609$), for $Re = 12,000$.
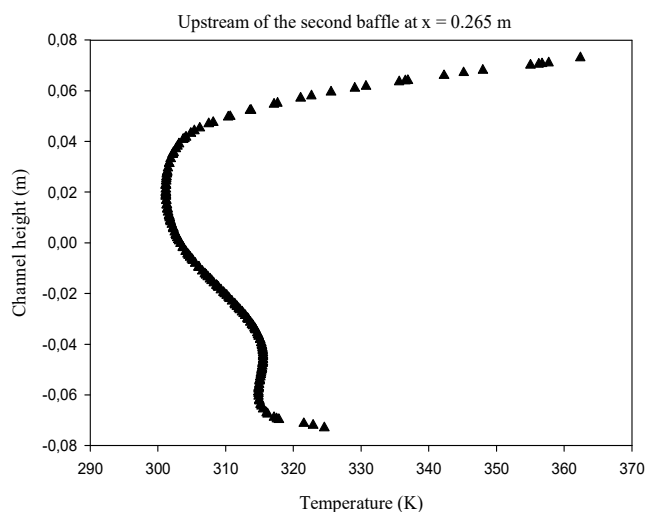

Fig. 13. Profiles of fluid temperature before the second S-baffles at $x = 0.265$ m (or $x/H = 1.815$), for $Re = 12,000$.
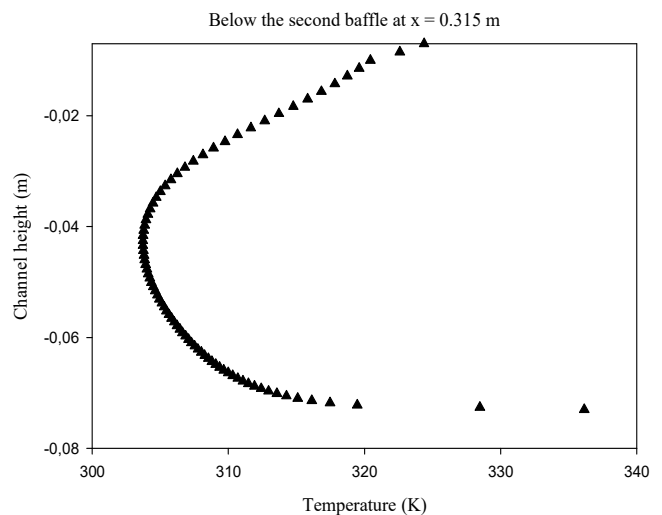

Fig. 14. Profiles of fluid temperature under the second S-baffles at $x = 0.315$ m (or $x/H = 2.157$), for $Re = 12,000$.

The distribution of temperature profiles between the lower and upper two S-baffles is shown in Fig. 12, at $x = 0.235$ m from the entrance of the channel or 0.319 m from its outlet. As expected, the temperature is very high near the hot walls, especially at the bottom of the channel, next to the base of the first S-baffle, and near the recycling cells, also near the right side of the same fin in contact with the hot upper channel wall, while the main current is accompanied by high speeds and very low temperatures.

On the front of the second S-baffle, at the cross-site $x = 0.265$ m from the entrance of the channel or 0.289 m from its outlet, 0.071 m after the first S-baffle or 0.045 m before the upper S-baffle, the temperature values are very important in the region between the top surface of the channel and the upper left side of the second S-baffle due to the presence of a small area of the recycling cells due to the decrease in the pressure in this aspect of the channel while the temperature in the high velocity areas decreases in the main path of the current and then rises near the right side of the first S-baffle due to the extension of the recycling cells to the second S-baffle, see Fig. 13.

The temperature profiles below the upper S-fin are shown in Fig. 14. In the axial site $x = 0.315$ m, extending from the bottom edge of the second S-fin to the upper surface of the bottom wall of the channel, the temperature decreases in a circular manner, especially in the central region of this area, due to the significant increase in air velocity due to the decrease in the flow area, as well as the efficiency of recycling cells in the back areas of the first S-fin, while air particle temperatures rise near hot surfaces as shown in Fig. 10 but with flat temperature profiles.

In the back of the second S-fin on the site $x = 0.365$ m, where resides the largest area for recycling as a result of the large decrease in pressure, temperature rises. This augmentation increases near the lower right hot area for this same S-fin, then the values of the temperature goes down at the bottom of the channel where the mainstream of air exists, see Fig. 15. In the central region between the second and third S-fins, at the location $x = 0.38$ m of the channel entrance, 0.06 m before the second lower S-fin, and 0.174 m from the channel outlet, the temperature is high in the upper side of the channel due to continuous circulation of the air current in the recycling cells and thus more absorption of thermal energy. This increase in temperature is indicative of the length of the recycling cells behind the second S-fin next to the upper area of the third S-fin, while the temperature in the middle of the site decreases where the main current is, because of the increase in speed due to the rise in pressure due to the presence of fins. We also record a temperature rise near the lower left side of the third S-fin, see Fig. 16.

Change in the temperature of the air particles near the left side of the third S-fin is shown in Fig. 17 at $x = 0.395$ m position. The temperature values are reduced by increasing the flow velocity in the vicinity of the upper area of the third S-fin as shown in Fig. 18 at $x = 0.445$ m, while the temperature rises as the current approaches the left side of this same S-fin, where the velocity decreases as a result of the pressure drop and formation of small recirculation cells in the lower area of the considered S-baffle.
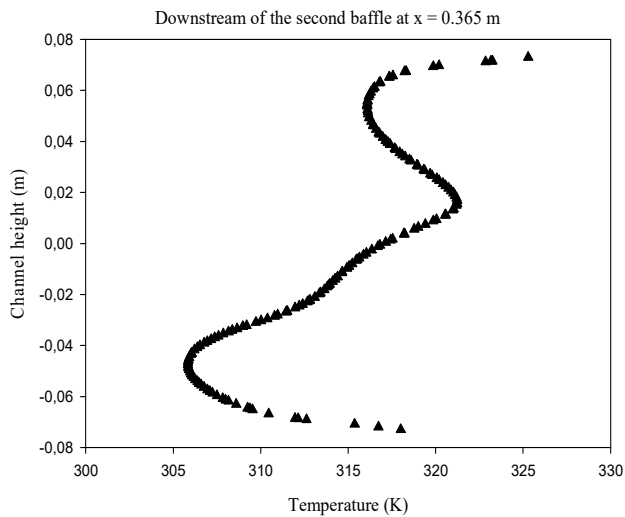
Fig. 15. Profiles of fluid temperature after the second S-baffles at $x = 0.365$ m (or $x/H = 2.5$), for $Re = 12,000$.
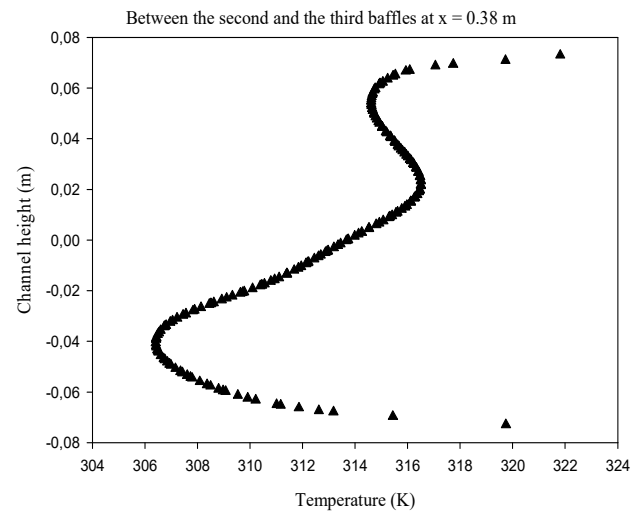

Fig. 16. Profiles of fluid temperature between the second and the third S-baffles at $x = 0.38$ m (or $x/H = 2.602$), for $Re = 12,000$.
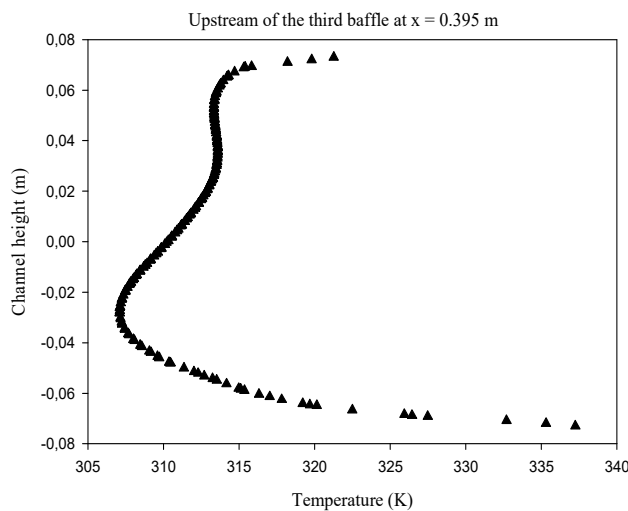

Fig. 17. Profiles of fluid temperature upstream of the third S-baffle at $x = 0.395$ m (or $x/H = 2.705$), for $Re = 12,000$.
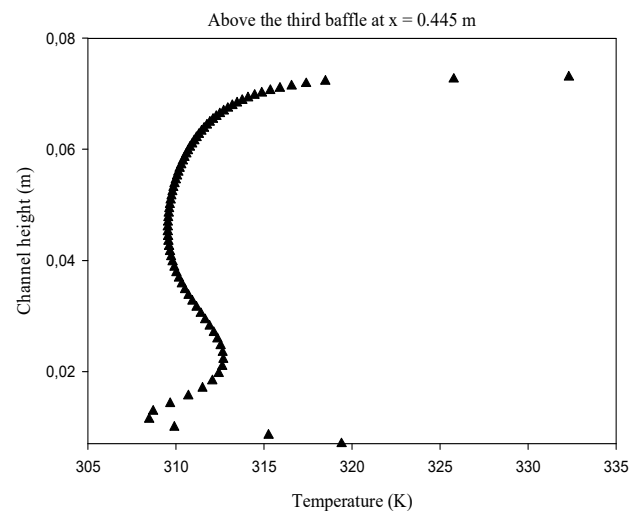

Fig. 18. Profiles of fluid temperature above the third S-baffle at $x = 0.445$ m (or $x/H = 3.047$), for $Re = 12,000$.
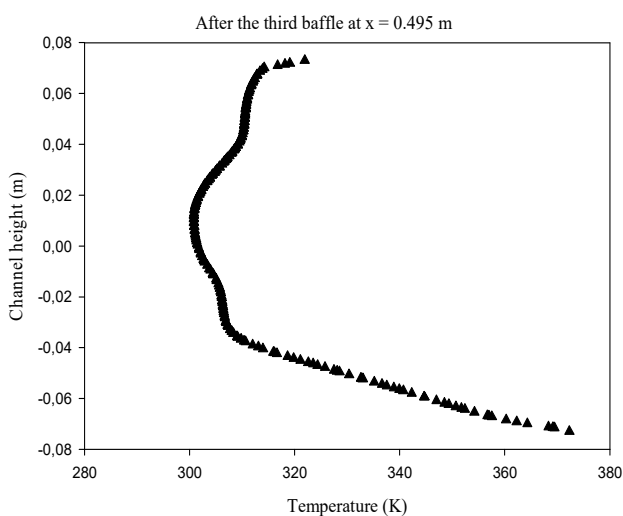

Fig. 19. Profiles of fluid temperature downstream of the third S-baffle at $x = 0.495$ m (or $x/H = 3.39$), for $Re = 12,000$.
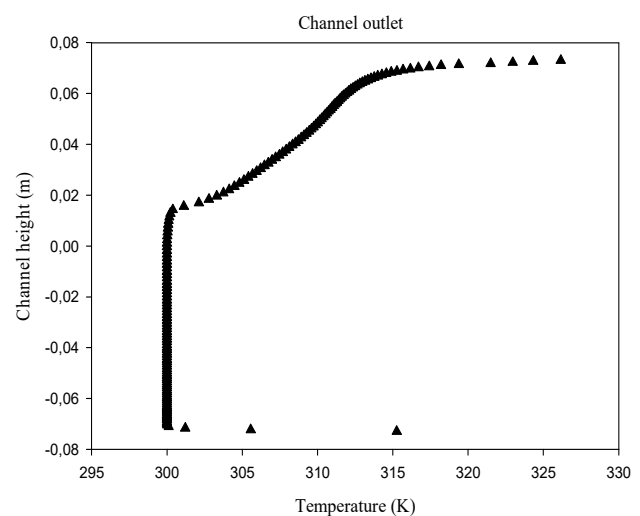
Fig. 20. Profiles of fluid temperature at the channel exit, $x = L$ (or $x/H = 3.794$) for $Re = 12,000$.

Behind the third S-fin, exactly at the cross-site $x = 0.495$ m of the channel entrance and as shown in Fig. 19, the temperature is inversely proportional to the flow velocity, where it rises when the speed decreases, especially in the recycling areas in the bottom of the channel on the right side of the S-fin, as expected. While the temperature in the upper part of the channel decreases as a result of the high speed rise.

(a) at the lower wall of the channel   (b) at the upper wall of the channel
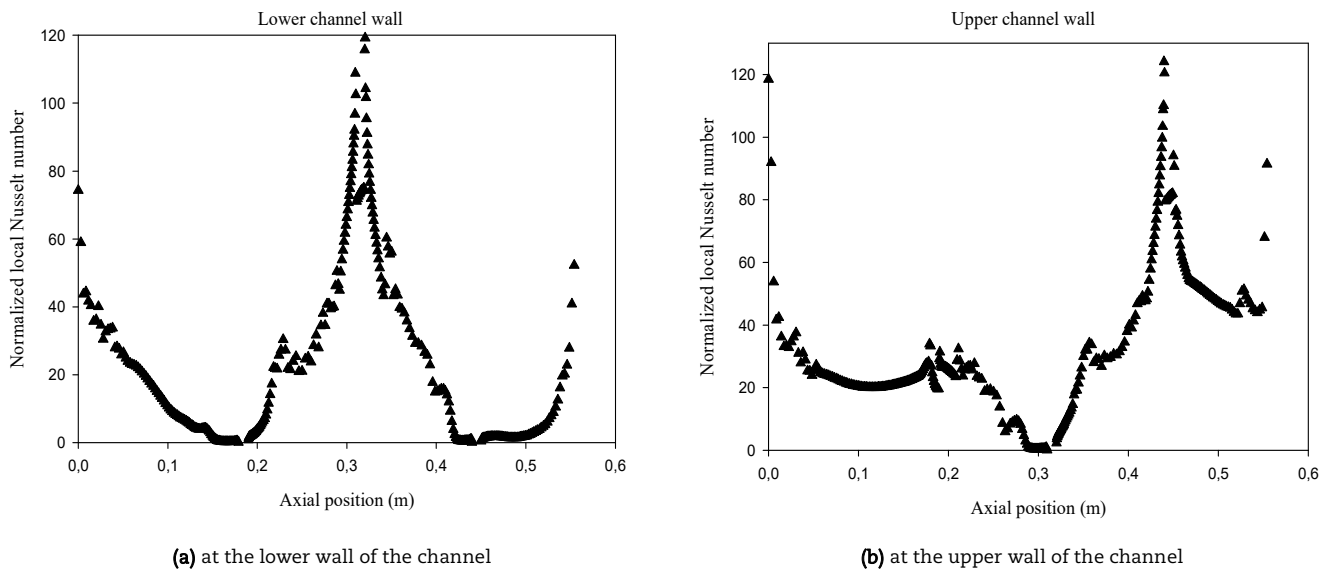
Fig. 21. Profiles of Nu_x/Nu_0 for $Re = 12,000$.

(a) at the lower wall of the channel   (b) at the upper wall of the channel
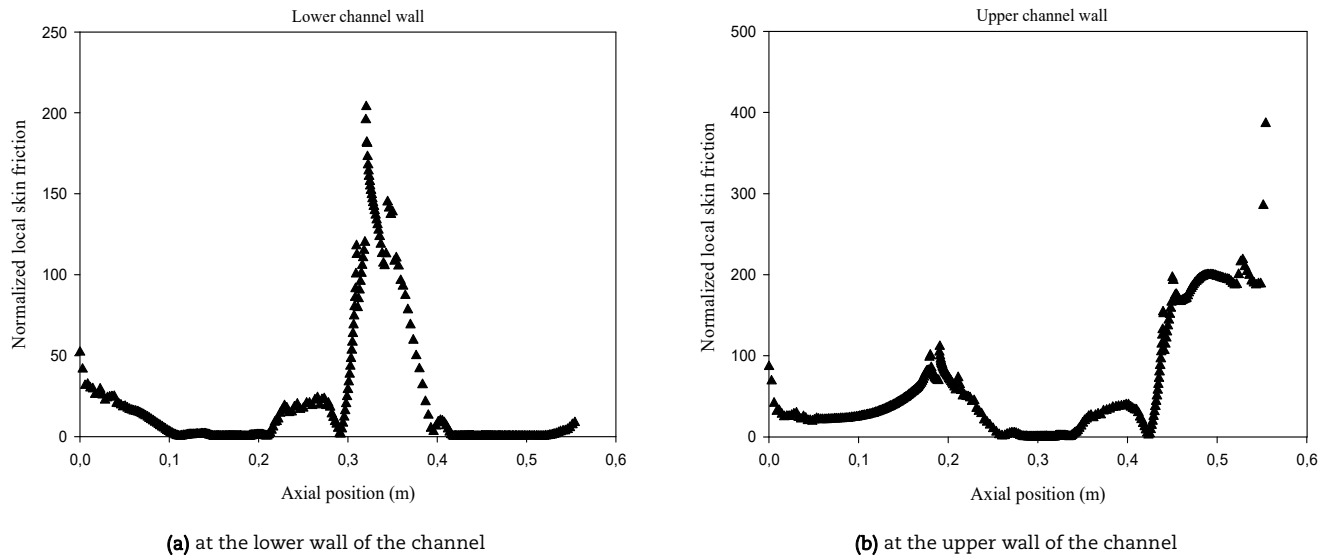
Fig. 22. Profiles of Cf/f_0 for $Re = 12,000$.
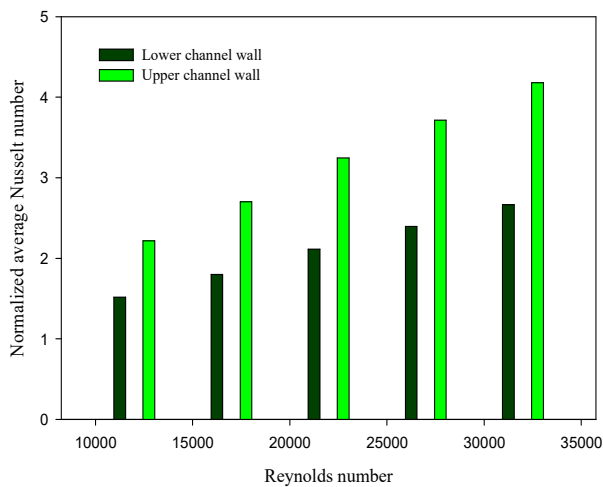
Fig. 23. Profiles of Nu/Nu_0 for various Re values.   **Fig. 24.** Profiles of f/f_0 for various Re values.
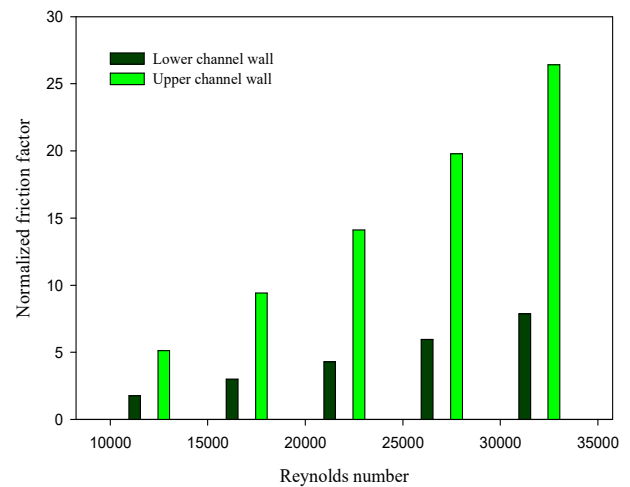
Near the outlet of the channel, at $x = 0.554$ m from its entrance, temperatures drop in the lower part of the channel as recycling cells do not extend to the outlet of the channel. On the upper side, temperature is important due to the presence, effectiveness and extension of the recycling cells after the second S-fin to the third S-fin as shown in Fig. 20.
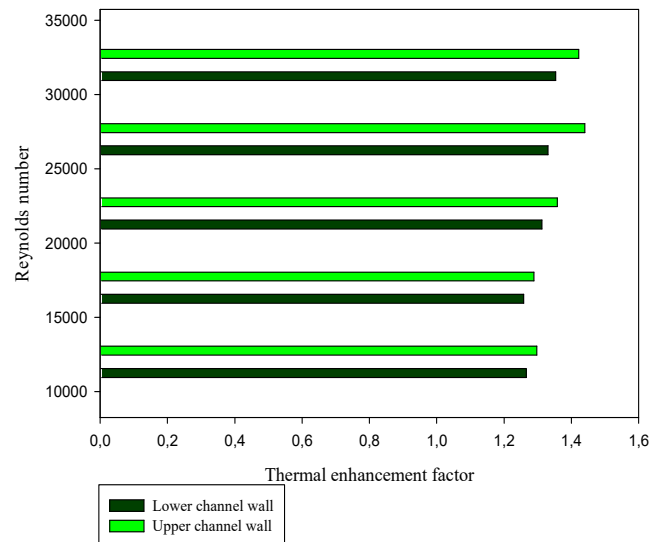
Fig. 25. *TEFs* for various *Re* values.

The heat exchange curves in terms of normalized local Nusselt number (Nu_x/Nu_0) profiles are represented in Fig. 21a, along the top surface of the bottom wall of the channel. The Nusselt number values are decreased next to the two lower S-fins, because the air field is directed towards the upper part of the channel. Thus decreasing the contact between the hot surface and the heat transfer fluid, resulting in a weak heat exchange. While heat transfer rate values in the opposite side of the top S-fin increase due to the augmentation in pressure and velocity, and from the large friction in this aspect of the channel, and thus the exchange of heat is important.

Heat exchange values are important in areas with significant thermal gradients, particularly in regions corresponding to lower S-fins with high speeds due to high current pressure due to a decrease in the flow area. While heat exchange decreases next to the upper S-fin due to the stagnation of the air field in this area, see Fig. 21b.

Fig. 22a shows changes in the Cf/f_0 of the upper surface of the bottom wall of the channel as the air current passes from the input to its outlet. The Cf/f_0 value decreases when approaching the lower first S-fin, due to the extreme deviation of the current due to the same baffle towards the upper wall of the channel; there is a decrease in contact between the fluid and the bottom wall of the channel; decrease in the skin friction coefficient in this region. The Cf/f_0 value enhances behind this same first S-fin due to the presence of recirculation cells in this back region. Also, the Cf/f_0 value is very high along the bottom wall line, between the first and the third S-fins, a result of the flow deviation from the upper to the bottom, due to the presence of the second S-fin, thus an important skin friction. Then the Cf/f_0 value decreases on the left and right sides of the third S-fin, due to the fluid flows toward the top region of the channel.

The Cf/f_0 value rises in three major regions, Fig. 22b. The first, against the first S-fin, is the result of large velocity in this region due to the deviation of the flow towards the upper part of the channel from this same S-fin. Second, behind the second S-fin, due to the presence of recycling cells in this area of the channel. Third, near the right side of the third S-fin, due to the direction of the air current towards the upper surface of the channel, at very high speeds, while the Cf/f_0 decreases, on the points of separation, next to the second S-fin, and between the main current above the third S-fin and the reverse field behind the second S-fin.

The Nu/Nu_0 changes are shown in Fig. 23 for the upper and lower hot walls. The Nu/Nu_0 values improve with improving *Re* values, from 12,000 to 32,000. All Nu/Nu_0 values are greater than one, ranging from 1.518 to 2.666 on the bottom hot wall while from 2.218 to 4.180 on the top hot wall, for the range of *Re* used. This indicates the effectiveness of the S-type fins inside the smooth channel in order to raise its thermal transfer through its hot walls.

Mean friction values (f/f_0) are also presented in this study through the curves of Fig. 24. The f/f_0 values are increasing in the range of *Re* given. Analyzing Figs. 23 and 24, indicates that the upper hot wall has produced very high values in terms of Nu/Nu_0 and f/f_0 compared to those from the lower hot wall, due to the presence of two upper gaps with very high temperature gradient and speed values. While, we find, next to the second hot wall, only one gap as a result of the upper S-fin.

The thermo-hydrodynamic performance (*TEF*) curves due to the presence of S-fins are shown in Fig. 25. The performance values are approximately 1.265 and 1.297 on the lower and upper hot walls of the channel, respectively, in the case of the minimum value of *Re*. As the *Re* changes, from 12,000 to 32,000, performance values improve to about 1.353 and 1.421 for the lower and upper hot walls, respectively. All *TEF* values are greater than the unit, indicating the advantage of using the S-shaped fins to increase the thermal and dynamic performance across the smooth channels, as an enhanced passive method.

5. Conclusion

The main results of the present numerical simulation showed that:
- The temperature gradient raised in three major regions. First, against first S-fin. It is the result of large friction in this region due to deviation of flow towards the upper part of channel from the same S-fin. Second, behind the second S-fin, due to the presence of recycling cells in this area of the channel. Third, near the right side of the third S-fin, due to the direction of the air current towards the upper surface of the channel, at very high speeds.
- The thermal gradient decreased, at the points of the flow separation, next to the second S-fin, and between the main current above the third S-fin and the reverse field behind the second S-fin.
- The heat transfer rate values were decreased next to the two lower S-fins, because the airfield is directed towards the upper part of the channel, thus decreasing the contact between the hot surface and the heat transfer fluid, resulting in a weak heat exchange.
- The heat transfer rate values on the opposite side of the top S-fin increased due to the augmentation in pressure and velocity, and from the large friction in this aspect of the channel, and thus the exchange of heat is important.

- Heat transfer values are important in areas with significant thermal gradients, particularly in regions corresponding to lower S-fins with high speeds due to high current pressure due to a decrease in the flow area. While heat transfer decreases next to the upper S-fin due to the stagnation of the airfield in this area.
- The Nu/Nu_0 values improved with improving Re values, from 12,000 to 32,000. All Nu/Nu_0 values are higher than one, ranging from 1.518 to 2.666 on the hot bottom wall, while from 2.218 to 4.180 on the top hot wall, for the range of Re used. This indicates the effectiveness of the S-type fins inside the smooth channel in order to raise its thermal transfer through its hot walls.
- The f/f_0 values are increasing in the range of Re given. The analysis of the heat transfer and friction loss also indicated that the hot upper wall has produced very high values in terms of Nu/Nu_0 and f/f_0 compared to those from the lower hot wall, due to the presence of two upper gaps with very high-temperature gradient and speed values.
- All TEF values are higher than the unit, indicating the advantage of using the S-shaped fins to increase the thermal and dynamic performance across the smooth channels, as an enhanced passive method.

Author Contributions

A.J. Chamkha proposed the physical model; Y. Menni simulated the computational domain numerically; H. Ameur analyzed the numerical results. The manuscript was written through the contribution of all authors. All authors discussed the results, reviewed, and approved the final version of the manuscript.

Conflict of Interest

The authors declared no potential conflicts of interest with respect to the research, authorship, and publication of this article.

Funding

The authors received no financial support for the research, authorship, and publication of this article.

Nomenclature

b	Inlet-upper wall-mounted S-fin distance [m]	S	Source term
c	Exit-upper wall-mounted S-fin distance [m]	T	Temperature [K]
Cf	Skin friction coefficient	T_{in}	Inlet fluid temperature [K]
$C_{1\varepsilon}$	Constant used in the standard k-ε model	T_w	Channel wall temperature [K]
$C_{2\varepsilon}$	Constant used in the standard k-ε model	S	Source term.
$C_{3\varepsilon}$	Constant used in the standard k-ε model	TI	Turbulent intensity [%]
C_μ	Constant used in the standard k-ε model	u	X-velocity of fluid [m/s]
d	Exit-second lower wall-mounted S-fin distance [m]	U_{in}	Inlet fluid velocity [m/s]
D_h	Aeraulic diameter of rectangular channel [m]	v	Y-velocity of fluid [m/s]
f	Friction factor for the channel with S-fins	V	Mean velocity of fluid [m/s]
f_0	Friction factor for the smooth channel with no fin	w	S-fin thickness [m]
h	S-fin height [m]	W	Channel width
H	Channel height [m]	ΔP	Pressure drop [Pa]
k	Turbulent kinetic energy [m²/s²]	ρ	Fluid density [kg/m³]
L	Channel length [m]	ε	Turbulent dissipation rate [m²/s³]
P	Pressure [Pa]	Γ	Turbulent diffusion coefficient
P_{atm}	Atmospheric pressure [Pa]	μ_e	Effective viscosity [kg/m-s]
Pr	Prandtl number	μ_l	Laminar viscosity [kg/m-s]
Re	Reynolds number	μ_t	Turbulent viscosity [kg/m-s]
s	Fin separation distance [m]	τ_w	Wall shear stress [Pa]

References

[1] Webb, B.W., Ramadhyani, S., Conjugate heat transfer in a channel with staggered ribs, *Int J Heat Mass Transf.*, 28, 1985, 1679-1687.

[2] Cheng, C.H., Huang, W.H., Numerical prediction for laminar forced convection in parallel-plate channels with transverse fin arrays, *Int J Heat Mass Transf.*, 34, 1991, 2739-2749.

[3] Menasria, F., Zedairia, M., Moummi, A., Numerical study of thermohydraulic performance of solar air heater duct equipped with novel continuous rectangular baffles with high aspect ratio, *Energy*, 133, 2017, 593-608.

[4] Singh, S., Chander, S., Saini, J.S., Heat transfer and friction factor correlations of solar air heater ducts artificially roughened with discrete V-down ribs, *Energy*, 36, 2011, 5053-5064.

[5] Mousavi, S.S., Hooman, K., Heat and fluid flow in entrance region of a channel with staggered baffles, *Energy, Conversion and Management*, 47, 2006, 2011-2019.

[6] Hwang, J.J., Liou, T.M., Heat transfer in a rectangular channel with perforated turbulence promoters using holographic interferometry measurement, *Int J Heat Mass Transf.*, 38, 1995, 3197-3207.

[7] Kiwan, S., Al-Nimr, M.A., Using porous fins for heat transfer enhancement, *ASME J Heat Transf.*, 123, 2000, 790-795.

[8] Kelkar, K.M., Patankar, S.V., Numerical prediction of flow and heat transfer in a parallel plate channel with staggered fins, *ASME J Heat Transf.*, 109, 1987, 25-30.

[9] Nasiruddin, Kamran Siddiqui, M.H., Heat transfer augmentation in a heat exchanger tube using a baffle, *Int J Heat Fluid Flow*, 28, 2007, 318-328.

[10] Zhao, H., Liu, Z., Zhang, C., Guan, N., Zhao, H., Pressure drop and friction factor of a rectangular channel with staggered mini pin fins of different shapes, *Exp Therm Fluid Sci.*, 781, 2016, 57-69.

[11] Demartini, L.C., Vielmo, H.A., Möller, S.V., Numeric and experimental analysis of the turbulent flow through a channel with baffle plates, *J Braz Soc Mech Sci Eng.*, 26, 2004, 153-159.

[12] Promvonge, P., Thianpong, C., Thermal performance assessment of turbulent channel flows over different shaped ribs, *Int Commun Heat Mass Transf.*, 35, 2008, 1327-1334.

[13] Wang, F., Zhang, J., Wang, S., Investigation on flow and heat transfer characteristics in rectangular channel with drop-shaped pin fins, *Propuls Power Res.*, 1, 2012, 64-70.

[14] Sripattanapipat, S., Promvonge, P., Numerical analysis of laminar heat transfer in a channel with diamond-shaped baffles, *Int Commun Heat Mass Transf.*, 36, 2009, 32-38.

[15] Saini, S.K., Saini, R.P., Development of correlations for Nusselt number and friction factor for solar air heater with roughened duct having arc-

shaped wire as artificial roughness, *Sol Energy*, 82, 2008, 1118-1130.

[16] Du, B.C., He, Y.L., Wang, K., Zhu, H.H., Convective heat transfer of molten salt in the shell-and-tube heat exchanger with segmental baffles, *Int J Heat Mass Transf.*, 113, 2017, 456-465.

[17] Lei, Y.G., He, Y.L., Li, R., Gao, Y.F., Effects of baffle inclination angle on flow and heat transfer of a heat exchanger with helical baffles, *Chem Eng Process*, 47, 2008, 2336-2345.

[18] Bekele, A., Mishra, M., Dutta, S., Effects of delta-shaped obstacles on the thermal performance of solar air heater, *Adv Mech Eng.*, 3, 2011, 103502.

[19] Wen, J., Yang, H., Wang, S., Xue, Y., Tong, X., Experimental investigation on performance comparison for shell-and-tube heat exchangers with different baffles, *Int J Heat Mass Transf.*, 84, 2015, 990-997.

[20] Dong, C., Zhou, X.F., Dong, R., Zheng, Y.Q., Chen, Y.P., Hu, G.L., Xu, Y.S., Zhang, Z.G., Guo, W.W., An analysis of performance on trisection helical baffles heat exchangers with diverse inclination angles and baffle structures, *Chem Eng Res Des.*, 2017. Doi: 10.1016/j.cherd.2017.03.027.

[21] Skullong, S., Thianpong, C., Jayranaiwachira, N., Promvonge, P., Experimental and numerical heat transfer investigation in turbulent square-duct flow through oblique horseshoe baffles, *Chem Eng Process*, 99, 2016, 58-71.

[22] Akbari, O.A., Afrouzi, H.H., Marzban, A., et al., Investigation of volume fraction of nanoparticles effect and aspect ratio of the twisted tape in the tube, *J Therm Anal Calorim.*, 129, 2017, 1911.

[23] Sriromreun, P., Thianpong, C., Promvonge, P., Experimental and numerical study on heat transfer enhancement in a channel with Z-shaped baffles, *Int Commun Heat Mass Transf.*, 39, 2012, 945-952.

[24] Patil, A.K., Saini, J.S., Kumar, K., Nusselt number and friction factor correlations for solar air heater duct with broken V-down ribs combined with staggered rib roughness, *J Renew Sustain Energy*, 4, 2012, 033122.

[25] Habib, M.A., Mobarak, A.M., Sallak, M.A., Abdel Hadi, E.A., Affify, R.I., Experimental investigation of heat transfer and flow over baffles of different heights, *ASME J Heat Transf.*, 116, 1994, 363-368.

[26] Al-Saif, A.S.J., Harfash, A.J., Perturbation-iteration algorithm for solving heat and mass transfer in the unsteady squeezing flow between parallel plates, *J Appl Comput Mech.*, 5(4), 2019, 804-815.

[27] King, E.M., Stellmach, S., Noir, J., Hansen, U., Aurnou, J.M., Boundary layer control of rotating convection systems, *Nature*, 457(7227), 2009, 301-304.

[28] Rajesh, R., Gowd, Y.R., Heat and mass transfer analysis on MHD peristaltic Prandtl fluid model through a tapered channel with thermal radiation, *J Appl Comput Mech.*, 5(5), 2019, 951-963.

[29] Davies, T.V., Planetary Atmospheres and Convection in Rotating Fluids, *Nature*, 180(4600), 1957, 1455-1461.

[30] Kezzar, M., Sari, M.R., Bourenane, R., Rashidi, M.M., Haiahem, A., Heat transfer in hydro-magnetic nanofluid flow between non-parallel plates using DTM, *J Appl Comput Mech.*, 4(4), 2018, 352-364.

[31] Zhao, L., Wang, B., Wang, R., Yang, Z., Aero-thermal behavior and performance optimization of rectangular finned elliptical heat exchangers with different tube arrangements, *International Journal of Heat and Mass Transfer*, 133, 2019, 1196-1218.

[32] Zhai, C., Islam, M.D., Simmons, R., Barsoum, I., Heat transfer augmentation in a circular tube with delta winglet vortex generator pairs, *International Journal of Thermal Sciences*, 140, 2019, 480-490.

[33] Guervilly, C., Cardin, P., Schaeffer, N., Turbulent convective length scale in planetary cores, *Nature*, 570(7761), 2019, 368-371.

[34] Yu, C., Zhang, H., Zeng, M., Wang, R., Gao, B., Numerical study on turbulent heat transfer performance of a new compound parallel flow shell and tube heat exchanger with longitudinal vortex generator, *Applied Thermal Engineering*, 164, 2020, 114449.

[35] Dutta, J., Kundu, B., Finite integral transform based solution of second grade fluid flow between two parallel plates, *J Appl Comput Mech.*, 5(5), 2019, 989-997.

[36] Korichi, A., Oufer, L., Numerical heat transfer in a rectangular channel with mounted obstacles on upper and lower walls, *International Journal of Thermal Sciences*, 44, 2005, 644-655.

[37] Herman, C., Kang, E., Comparative evaluation of three heat transfer enhancement strategies in a grooved channel, *Heat and Mass Transfer*, 37, 2005, 563-575.

[38] Read, P.L., Rotating convection on the edge, *Nature*, 457, 2009, 270-271.

[39] Manca, O., Nardini, S., Ricci, D., A numerical study of nanofluid forced convection in ribbed channel, *Applied Thermal Engineering*, 37, 2012, 280-292.

[40] Ndlovu, P.L., Numerical analysis of transient heat transfer in radial porous moving fin with temperature dependent thermal properties, *J Appl Comput Mech.*, 6(1), 2020, 137-144.

[41] Ooi, A., Laccarino, G., Durbin, P.A., Behnia, M., Reynolds average simulation of flow and heat transfer in ribbed duct, *International Journal of Heat and Fluid Flow*, 23, 2002, 750-757.

[42] Ortiz, L., Hernandez-Guerrero, A., Rubio-Arana, C., Romero-Mendez, R., Heat transfer enhancement in a horizontal channel by the addition of curved deflectors, *International Journal of Heat and Mass Transfer*, 51, 2008, 3972-3984.

[43] Singh, S., Dhiman, P., Analytical and experimental investigations of packed bed solar air heaters under the collective effect of recycle ratio and fractional mass flow rate, *Journal of Energy Storage*, 16, 2018, 167-186.

[44] Singh, S., Experimental and numerical investigations of a single and double pass porous serpentine wavy wiremesh packed bed solar air heater, *Renewable Energy*, 145, 2020, 1361-1387.

[45] Saleh, H., Siri, Z., Hashim, I., Role of fluid-structure interaction in mixed convection from a circular cylinder in a square enclosure with double flexible oscillating fins, *International Journal of Mechanical Sciences*, 161-162, 2019, 105080

[46] Launder, B.E., Spalding, D.B., The numerical computation of turbulent flow, *Computer Methods in Applied Mechanics and Engineering*, 3(2), 1974, 269-289.

[47] Dittus, F.W., Boelter, L.M.K., Heat transfer in automobile radiators of tubular type, *Univ. California, Berkeley, Publ. Eng.*, 1(13), 1930, 755-758.

[48] Petukhov, B.S., Heat transfer and friction in turbulent pipe flow with variable physical properties, *Advances in Heat Transfer*, 6, 1970, 503-564.

[49] Patankar, S.V., Numerical heat transfer and fluid flow, McGraw-Hill, New York, 1980.

[50] Leonard, B.P., Mokhtari, S., Ultra-sharp nonoscillatory convection schemes for high-speed steady multidimensional flow, NASA TM 1-2568, NASA Lewis Research Center, 1990.

[51] ANSYS Fluent 12.0, Theory Guide, Ansys Inc., 2012.

ORCID iD

Ali J. Chamkha https://orcid.org/0000-0002-8335-3121
Younes Menni https://orcid.org/0000-0003-1475-3743
Houari Ameur https://orcid.org/0000-0003-2087-7574